CrossMark

Sources of the Multi-Lane Type II Solar Radio Burst on 5 November 2014

M.S. Lv[1] · Y. Chen[1] · C.Y. Li[1] · I. Zimovets[2,3,4] ·
G.H. Du[1] · B. Wang[1] · S.W. Feng[1] · S.L. Ma[5]

Abstract We report the well-observed event of a multi-lane type II solar radio burst with a combined analysis of radio dynamic spectra and radio and extreme-ultraviolet (EUV) imaging data. The burst is associated with an EUV wave driven by a coronal mass ejection (CME) that is accompanied by a GOES X-ray M7.9 flare on 5 November 2014. This type of event is rarely observed with such a complete data set. The type II burst presents three episodes (referred to as A, B, and C), characterized by a sudden change in spectral drift, and contains more than ten branches, including both harmonic-fundamental (H–F) pairs and split bands. The sources of the three episodes present a general outward propagating trend. There exists a significant morphology change from single source (Episode A) to double source (Episode B). Episode C maintains the double-source morphology at 150 MHz (no imaging data are available at a lower frequency). The double-source centroids are separated by ∼ 300″ to 500″. The southeastern (SE) source is likely the continuation of the source of Episode A since both are at the same section of the shock (*i.e.* the EUV wave) and close to each other. The northwestern (NW) source is coincident with (thus, possibly originates from) the interaction of the shock with a nearby mini-streamer-like structure. Comparing

✉ Y. Chen
  yaochen@sdu.edu.cn

  M.S. Lv
  lvmaoshui@sdu.edu.cn

1 Shandong Provincial Key Laboratory of Optical Astronomy and Solar-Terrestrial Environment, Institute of Space Sciences, Shandong University, Weihai, Shandong 264209, China

2 State Key Laboratory of Space Weather, National Space Science Center, Chinese Academy of Sciences, Beijing 100190, China

3 International Space Science Institute – Beijing, Beijing 100190, China

4 Space Research Institute of the Russian Academy of Sciences, Profsoyuznaya St. 84/32, Moscow 117997, Russia

5 College of Science, China University of Petroleum, Qingdao, Shandong 266580, China

🌀 Springer

the simultaneously observed sources of the F and H branches of Episode A, we find that their centroids are separated by less than 200″. The centroids of the split bands of Episode B are cospatial within the observational uncertainties. This study shows the source evolution of a multi-lane type II burst and the source locations of different lanes relative to each other and to the EUV wave generated by a CME. The study indicates the intrinsic complexity underlying a type II dynamic spectrum.

Keywords Radio bursts, type II · Coronal mass ejections

1. Introduction

Multi-lane type II solar radio bursts, a special group of type II events, are defined according to their manifestation on radio dynamic spectra (the radio emission intensity map as a function of both time and frequency) (Payne-Scott, Yabsley, and Bolton, 1947; Nelson and Melrose, 1985; Robinson and Sheridan, 1982; Shanmugaraju *et al.*, 2005; Feng *et al.*, 2013, 2015). They are characterized by several distinct emission lanes that are narrow-band and slowly drifting in frequency. These lanes cannot be fully grouped into fundamental (F) and harmonic (H) counterparts (with a frequency ratio of ∼ 2) and split bands (with correlated or similar spectral features, see Du *et al.*, 2014, 2015, for the latest observational studies). The lanes usually have different drift rates, start times, spectral features, and intensity variations. Their onset times are expected to occur within a limited range of ∼ 10 minutes.

Mainly on the basis of the above-described spectral features, earlier studies surmised that different lanes may have different solar drivers, either being a flare blast-wave and a piston-driven shock of the flare-accompanying coronal mass ejection (CME), *i.e.* on a single-eruption basis, or different shocks driven by subsequent eruptions. It has also been conjectured that different parts of a single shock, such as its nose and flanks, can be sources of different lanes (Robinson and Sheridan, 1982; Gergely *et al.*, 1984; Shanmugaraju *et al.*, 2005; Cho *et al.*, 2007, 2008, 2011; Feng *et al.*, 2013, 2015). Statistical as well as case studies have been carried out to find clues to distinguish these scenarios.

For example, Shanmugaraju *et al.* (2005) have collected 38 multi-lane type II bursts observed from 1997 to 2003, and examined their association with flares and CMEs. They found that 90% of the events were associated with both flares and CMEs. It is well known that flares and CMEs often occur coincidentally (*e.g.* Zhang *et al.*, 2001; Song *et al.*, 2015). Thus, it is in general difficult, if not impossible, for a statistical study to distinguish the origin of different lanes on the basis of spectral data and a timing analysis. Earlier case studies led to controversial statements about the origin of different lanes of the same event. The well-known multi-lane type II radio burst on 31 December 2007 was analyzed by many groups of authors (*e.g.* Liu *et al.*, 2009; Gopalswamy *et al.*, 2009; Cho *et al.*, 2011; Feng *et al.*, 2013). These authors apparently agreed on the point that the type II burst as a whole was associated with the CME. The origin of different lanes of this type II burst has been investigated by Cho *et al.* (2011) and Feng *et al.* (2013). Cho *et al.* concluded that the first lane stemmed from the CME nose and the second lane from the CME flank that interacted with a nearby streamer, while Feng *et al.* concluded that both lanes were associated with CME interactions with nearby streamers, one from the southern part and the other from the northern part. This controversial result for the same event is largely attributed to the absence of direct-imaging data, not only at the EUV wavelengths or white light with the shock signature, but also at the radio frequencies for the emitting sources.

Feng *et al.* (2015) presented a combined analysis of simultaneous imaging data at the EUV passbands and radio-meter wavelengths of a multi-lane type II event on 16 February 2011. The EUV data were provided by the twin *Solar Terrestrial Relations Observatory* (STEREO: Howard *et al.*, 2008) spacecraft and the *Solar Dynamics Observatory* (SDO: Pesnell, Thompson, and Chamberlin, 2012), and the radio imaging data were obtained with the *Nançay Radioheliograh* (NRH: Kerdraon and Delouis, 1997). Using the three-perspective imaging data of the same shock structure, the authors were able to reconstruct the three-dimensional dome-like surface of the shock. They concluded that the three-lane type II event was associated with a single shock structure driven by the accompanying CME. All the three-lane sources were located at the western flank of the shock, two of them being on the northwestern flank and cospatial (within the observational uncertainties) with each other, while the other source was at the southwestern flank. They also pointed out that more multi-lane type II events needed to be examined for a complete understanding of their origin. Note that Zimovets and Sadykov (2015) analyzed the same event independently and reached similar conclusions.
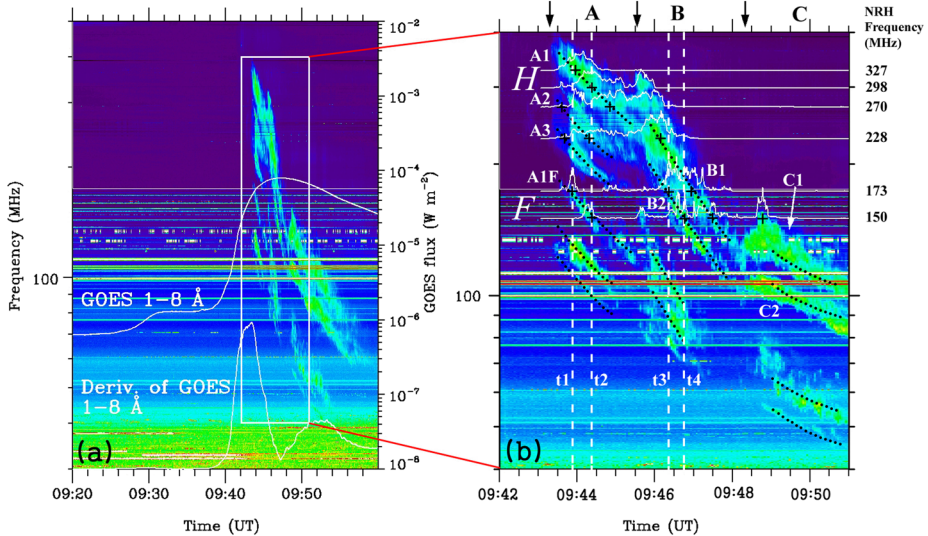
In this article we report a well-observed multi-lane type II burst. The dynamic spectrum of the burst contains more than ten clearly separated emission branches, which can be grouped into three episodes according to sudden changes of the spectral drifting rates. Both H–F branches and obvious split bands are presented. The associated eruption was simultaneously recorded by the *Atmospheric Imaging Assembly* (AIA: Lemen *et al.*, 2012) onboard the SDO at various EUV passbands and the NRH at different meter wavelengths. Different lanes, including H–F and band-split counterparts, mostly the H branches of the first two episodes, are imaged by the NRH. This allows us to compare and deduce their source locations relative to each other and to the EUV wave structure, and shed light on their origin. The next section presents the dataset analyzed and an overview of the event. The third section focuses on the EUV wave and its association with the flare and CME. The fourth section analyzes the radio spectral and imaging data, and the fifth section presents a combined analysis of the simultaneously observed radio and EUV data. Our summary and discussion are presented in the last section.

2. Observational Data and Event Overview

The radio dynamic spectrum of the multi-lane type II burst was obtained from a combination of the Learmonth station of the USAF *Radio Solar Telescope Network* (RSTN; $30 - 145$ MHz)[1] and the *Observation Radio Fréquences pour l'Etude des Eruptions Solaires* (ORFEES, $145 - 500$ MHz).[2] The radio sources were imaged by NRH at six frequencies (150, 173, 228, 270, 298, and 327 MHz). The total flux densities (and brightness temperature) are calibrated with one of the strongest wide-band radio sources in the sky (the radio galaxy Cygnus A, see Baars *et al.*, 1977; Kerdraon and Delouis, 1997). This is completed with a self-calibration process. The spatial resolution of NRH images is determined by the half-power beam width of the system, which can be obtained with the standard NRH software included in the SolarSoftware package. During our event, the half-power beam sizes are found to be $282''$ (major axis of the beam ellipse) and $109''$ (minor axis of the beam ellipse) at 327 MHz, $307''$ and $119''$ at 298 MHz, $339''$ and $132''$ at 270 MHz, $402''$ and $156''$ at 228 MHz, $523''$ and $206''$ at 173 MHz, and $597''$ and $237''$ at 150 MHz.

---

[1] ftp://ftp.ngdc.noaa.gov/STP/space-weather/solar-data/solar-features/solar-radio/rstn-spectral.

[2] http://secchirh.obspm.fr/downloadOrfeesHR1.php.

Figure 1 Dynamic spectra of the multi-lane type II radio burst. (**a**) Spectrum given by combining the data from the Learmonth Solar Observatory (30 – 145 MHz) and the ORFEES (145 – 500 MHz), overlaid by the GOES 1 – 8 Å flux and its time derivative. (**b**) Enlargement of the region within the *white box* of panel **a**. In panel **b**, the *white curves* present the total flux density of the six NRH frequencies. The frequency corresponding to these curves is indicated in the vertical axis to the right. The plus signs are selected local maxima of the NRH intensity. The *black dotted lines*, given by the linkage of these signs, represent the backbones of the type II H branches. The *lines* on the F branches are given by the division of these lines over 1.97. The *three black arrows* at the top of the panel denote the start times of the three episodes (A – C), and the *four vertical white dashed lines* indicate the times (t1 – t4) selected for further analysis.

The EUV images of the eruption were taken by SDO/AIA. Other data used here include the soft X-ray (SXR) light curve from the *Geostationary Operational Environmental Satellite* (GOES) and coronal white-light images from the *Large Angle and Spectrometric Coronagraph* (LASCO: Brueckner *et al.*, 1995) C2 onboard the *Solar and Heliospheric Observatory* (SOHO: Domingo, Fleck, and Poland, 1995).

Figure 1a shows the dynamic spectrum of the multi-lane type II burst overlaid by the GOES SXR curves from 09:30 to 10:00 UT. The enlargement of the rectangle region is shown in Figure 1b (from 09:42 to 09:51 UT), overlaid by the total flux curves at the six NRH observing frequencies. The type II burst starts at ∼ 09:43 UT and ends at ∼ 09:57 UT, lasting for ∼ 14 minutes. The most prominent feature of the radio burst is that it is composed of multiple branches and shows a change in spectral drifting rate with time. According to the drifting rates and the sequence of appearance, we separate the type II burst into three episodes, referred to as A, B, and C. Their onset times (∼ 09:43:20, 09:45:31, and 09:48:20 UT) are marked at the top of the spectrum in Figure 1b.

The type II burst was associated with an M7.9 flare originating from NOAA active region (AR) 12205 (N15 E69) located near the northeastern limb on 5 November 2014. The start and peak times of the flare are 09:26 and 09:47 UT, respectively. It was accompanied by a partial-halo CME with a central position angle of ∼ 87° and a linear speed of ∼ 386 km s^{-1}, according to the Coordinated Data Analysis Workshops (CDAW) online data.[3] The flare took place during the *Reuven Ramaty High Energy Solar Spectroscopic Imager* (RHESSI)

---

[3]https://cdaw.gsfc.nasa.gov.
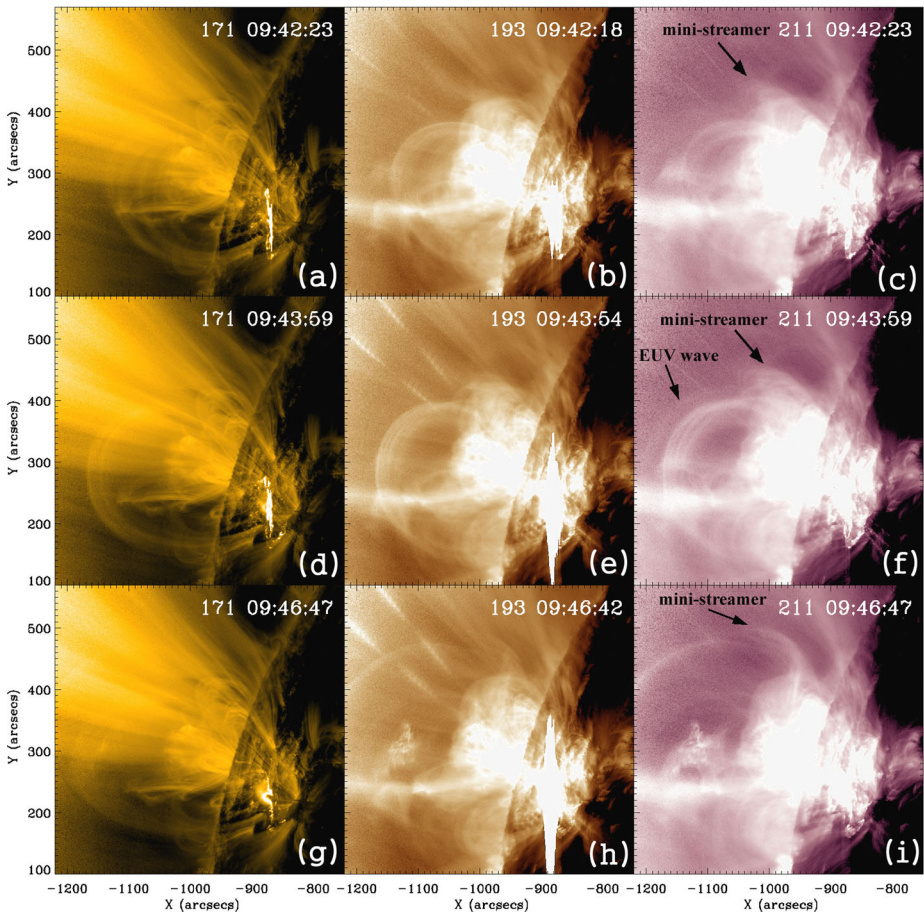
Figure 2 AIA EUV images of the eruption at 171, 193, and 211 Å, observed before (**a**–**c**) and during (**d**–**i**) the type II bursts. The *arrows* in the *right panels* point to the EUV wave front and the mini-streamer-like structure that is strongly disturbed by the eruption. An animation is available as online supplementary material.

night, so there are no RHESSI hard X-ray (HXR) data for this event. We calculated the time derivative of the GOES SXR data at $1-8$ Å (plotted in Figure 1a) to approximate the HXR data and determine the timing of the flare impulsive phase, according to the Neupert effect (Neupert, 1968). The impulsive phase of the flare starts at $\sim$ 09:39 UT, peaks at $\sim$ 09:43 UT, and ends at $\sim$ 09:47 UT. The type II burst is basically coincident with the flare impulsive phase. Since the type II burst is also closely associated with the CME as described below, it is not possible to tell the exact driver of the type II burst from a timing analysis alone.

In Figure 2 (and the accompanying movie) we show the AIA EUV images of the eruption at 171, 193, and 211 Å. The times of the images presented in Figure 2 are selected to be just before (Figures 2a–c) and during (Figures 2d–i) the type II burst. The eruption is characterized by a set of initially static loop structures that are blown outward by a rapidly moving loop-like structure from underneath. The eruption contains a slowly moving bright core (also observed at the low-temperature 304 Å channel of AIA, indicating the presence of cool-dense prominence material). It causes a strong disturbance of the nearby coronal
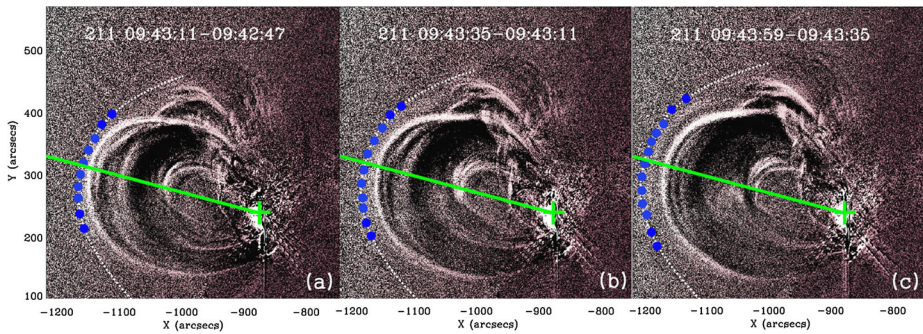
Figure 3 Measured (*blue dots*) and fitted (*white dashed lines*) profiles of the EUV wave front driven by the CME. The difference images obtained at 211 Å are used for the measurements, and the fitting curves are given by the symmetrical bow-shock assumption (see text for details). The *green lines* represent the presumed symmetrical axis of the wave structure, starting from the center of the AR (the *plus sign*). The accompanying animation is mentioned in Figure 2.

structures, in particular, a mini-streamer-like bright structure (*i.e.* closed loops underneath a collimated ray-like structure) on the northern side (see the black arrows in Figures 2c, f, and i). Together with some structures farther away from the ejecta, the mini-streamer-like structure is pushed aside without direct contact with the bright ejecta. This indicates the existence of a fast-mode wave (or shock) ahead of the eruptive ejecta, which can propagate through magnetic structures. The wave is described in more detail in the next section.

3. AIA EUV Wave and the Driver of the Type II Burst

By examining the EUV data, we recognized a rather diffuse EUV wave structure ahead of the bright ejecta (indicated with a black arrow in Figure 2f). The wave structure is most clearly observed at 211 Å of the AIA data and best seen in the accompanying movie (from 09:43:11 to 09:44:23 UT). According to the movie, the strong interaction of the EUV wave and the mini-streamer-like structure starts at a time between 09:44:47 and 09:45:35 UT.

To further reveal the evolution of the EUV wave, in Figure 3 we show the difference images of AIA 211 Å recorded at three times (09:43:11, 09:43:35, and 09:43:59 UT). These are the moments at which the EUV wave can be clearly recognized. The profiles of the front are delineated with blue dots. The extension of the wave front is consistent with the kink of the stalk at the top of the mini-streamer-like structure, indicating that the propagation across the field of the EUV wave is the cause of the disturbance of this structure.

Since the EUV wave is only clearly observable at the three times, extrapolations are required to deduce the wave locations at other times. Following Chen *et al.* (2014) and Feng *et al.* (2015), we assumed that the wave profile can be approximated by a symmetrical bow shock that can be modeled as follows:

$$Z = h - \frac{d}{s} \times \left(\frac{\sqrt{X^2 + Y^2}}{d} \right)^s, \tag{1}$$

where h indicates the shock apex height away from the center of the AR (see Figure 2), s determines the bluntness of the shock, and d controls the width of the shock. The equation is given in a local Cartesian coordinate system, and the center of the AR is taken to be the

Figure 4 Measured distances of the EUV wave fronts away from the center of the AR along the axis, together with the measurements of the CME fronts and the type II sources corresponding to those shown in Figure 6. The speed of the EUV wave front and the radio sources are presented by linearly fitting the distance–time measurements (indicated by the *red* and *purple dashed lines*, respectively). Only the Episode A sources and the SE sources of Episode B and C are selected for the radio source fitting. The time derivative of the GOES $1-8$ Å flux is overlaid to show the impulsive phase of the flare.
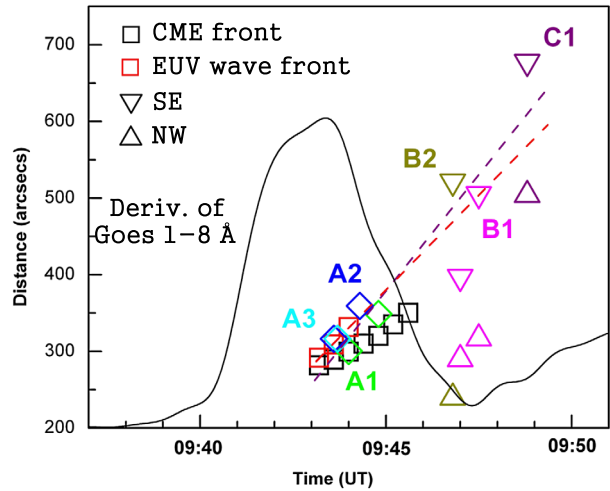
origin; the symmetrical axis points to the bow apex along Z, and X and Y define the plane perpendicular to Z. For our event, the data are not available from perspectives different from the Earth (SDO). Therefore, for simplification, we set X to point at Earth. This is equivalent to assuming that the symmetrical axis of the EUV wave is in the sky plane, *i.e.* the $Y-Z$ plane. Thus the wave profile in the sky plane can be described using the above equation by setting X to zero. This is a reasonable simplification since the event erupted near the solar limb and the projection effect on the location of the wave front is likely not significant. The green lines in Figure 3 are taken to be the symmetrical axis of the ejecta in the projection plane, starting from the center of the AR. Along this line, we measured the distances of the EUV wave front away from the center of the AR. The results are shown in Figure 4. The linearly fitted propagation speed of the EUV wave is ~ 600 km s^{-1}. We then used the above equation to fit the measured data points of the EUV wave fronts. The obtained best-fitted wave profiles are overplotted on the EUV difference images with white dotted lines in Figures 3a–c.

To analyze the flare-CME relationship with the type II burst, in Figure 4 we also show the position measurements of the CME front and the centroids of some selected radio sources observed by the NRH (shown in Figure 6). The derivative of GOES $1-8$ Å profile is also plotted. The EUV wave is immediately ahead of the CME front, and its distance and speed are consistent with those deduced using the radio sources. The type II onset ($\sim 09{:}43$ UT) and the appearance of the EUV wave are both coincident with the flare impulsive phase. As we described, it is not possible to determine the exact driver of the EUV wave from a time analysis alone (the EUV wave is closely associated with the type II sources, as we show below, therefore we refer to it as the shock wave). We therefore resorted to the imaging data presented in Figures 2 and 3. Around 09:43 UT, the EUV wave appears in the AIA field of view (FOV), immediately ahead of the CME ejecta (the bright loop or bubble-like structure). The EUV wave nicely envelopes the front of the ejecta. In other words, the wave and the bright CME front share a very similar shape. The stand-off distance (from the EUV shock to the ejecta front) is smaller at the center and larger at the sides. In general, the EUV wave (when recognizable) and the CME ejecta move outward together (*i.e.* with similar dynamics). These observations favor the explanation that the EUV shock wave is driven by the CME, not by the flare.
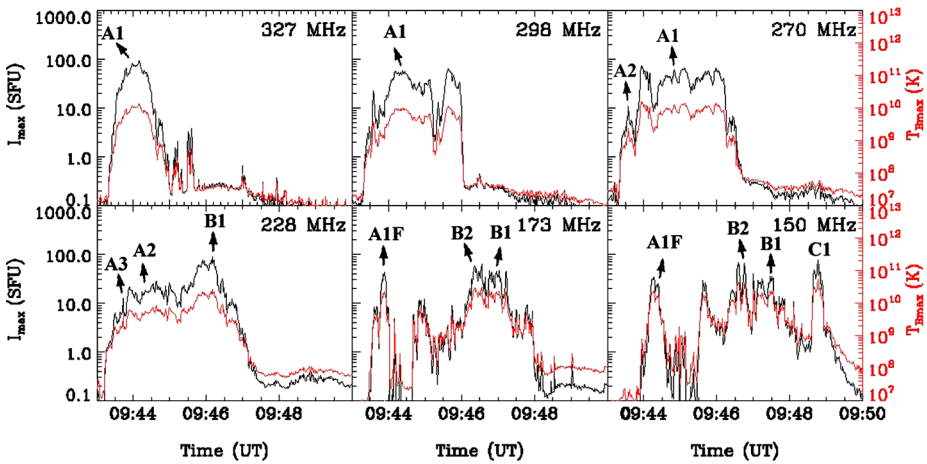
Figure 5 Maxima of the flux intensity (I_{max}, *black*) and the brightness temperature (T_{Bmax}, *red*) of the radio bursts obtained by NRH at six frequencies. The corresponding labels of various type II branches are indicated.

## 4. Analysis of the Radio Spectral and Imaging Data

Figure 1b shows that the NRH flux curves (the six white curves) and the ORFEES dynamic spectrum reflect a consistent variation of the radio flux. The plus signs represent the local maxima of the NRH fluxes. By linking them, we delineated the backbones of the type II burst. This was done only for the H branches. These backbone curves were then divided by 1.97 to derive those for the corresponding F branches. The derived curves are well consistent with the observed branches at lower frequencies, indicating that they indeed represent the F branches. Episode A consists of three H–F pairs and Episodes B and C consist of two clearly discernible H–F branches each. According to their H–F nature and order of frequencies, the observed H branches are referred to as A1, A2, A3, B1, B2, C1, and C2, and the F branches as A1F, A2F, A3F, B1F, B2F, C1F, and C2F. In Figure 1b we mostly label the branches using NRH imaging data.

The two branches B1-B2 (and C1-C2, and their fundamental counterparts) show a similar spectral variation, and their frequency ratio is much lower than 2. This indicates that B1-B2 (and C1-C2) are split bands (Nelson and Melrose, 1985; Vršnak *et al.*, 2001; Du *et al.*, 2015; Vasanth *et al.*, 2014). From the spectral data, it is hard to tell which two of the three branches of Episode A (A1, A2, A3) may correspond to split bands. We return to this point on the basis of the NRH source image data.

In Figure 5 we plot the temporal profiles of the maxima of the radio flux intensity (I_{max}) and the corresponding brightness temperature (T_{Bmax}) at the six NRH frequencies. The radio intensity peaks corresponding to the backbones of the type II burst are highlighted. For different branches, the maxima of I_{max} vary from $\sim 10–90$ solar flux units (SFU) and those of T_{Bmax} vary from $\sim 0.2–5 \times 10^{10}$ K. The high T_B indicates a very strong coherent plasma emission (Ginzburg and Zhelezniakov, 1958; Melrose, 1980).

Such high T_Bs can also be seen in the NRH images at different frequencies, as shown in Figure 6 and the accompanying movie. In Figure 6 the panels are arranged according to the sequence of episodes. Figures 6a – e show Episode A, Figures 6f – h show Episode B, and the last panel shows Episode C. Each panel corresponds to a plus sign (a combination of frequency and time), as plotted in Figure 1b, that is representative of the local maximum of
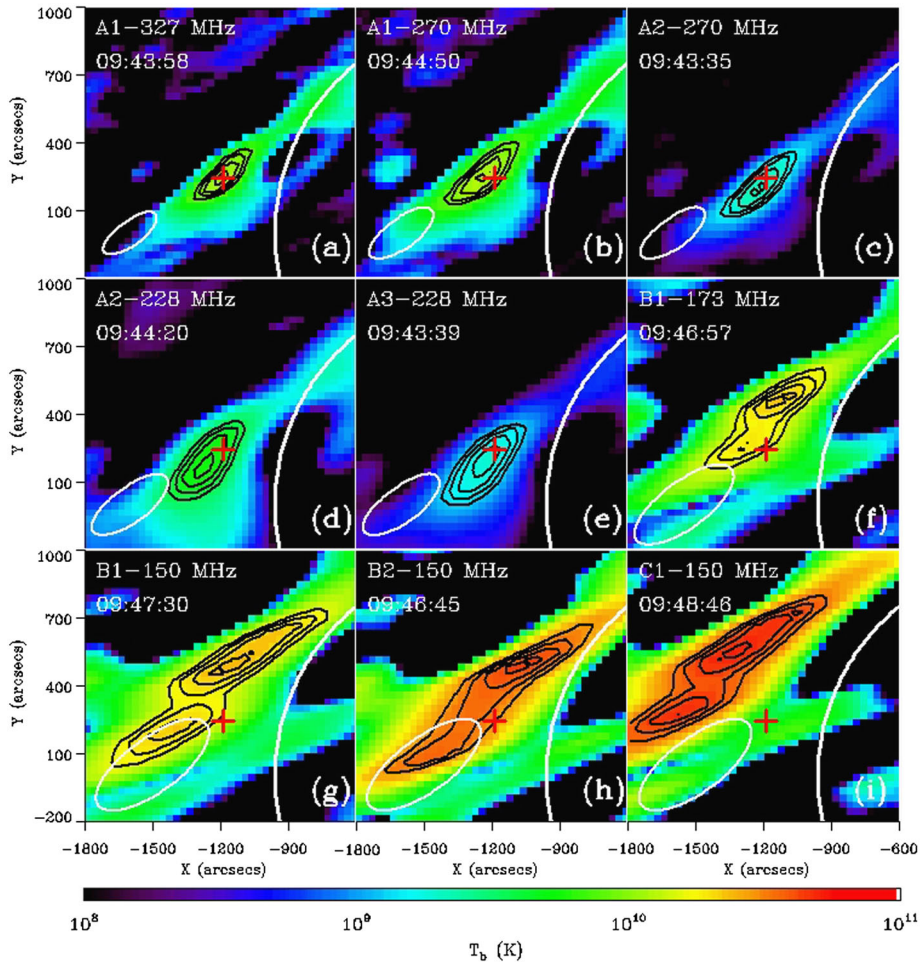
Figure 6 NRH images at different frequencies for different lanes. The time and frequency combination correspond to those of the *black plus sign*, as plotted in Figure 1b. The *contours* are given by the 65, 75, 85, and 95% levels of T_{Bmax}, and the red plus sign denotes the centroid (T_{Bmax}) of the A1 source at 327 MHz. The *beam ellipse* is shown for each panel. An animation is available as electronic supplementary material.

the NRH radio flux intensity. The red plus in each panel represents the centroid of the A1 source at 327 MHz and 09:43:58 UT, plotted for convenience of comparison.

The most interesting feature of Figure 6 is the morphology change of the radio sources from Episode A to Episodes B and C. Episode A has a usual single-source morphology, while the sources of both B and C show a peanut-like double-source morphology. The double sources are referred to as the SE and NW source hereafter. Note that Episode C is only imaged at the lowest working frequency (150 MHz) of the NRH, so it remains unknown whether the double-source morphology is maintained later. The separation of the centroids of the double sources varies from $\sim 300''$ to $500''$, which is comparable to or smaller than the corresponding NRH beam widths at 150 and 173 MHz. In addition, the two sources are persistent and at a close level of T_B. These observations indicate that the double-source morphology is real. The SE source of Episode B is very close to the source of Episode A.

This suggests that the SE source of Episode B and C may be the continuation of Episode A source; in other words, they have the same origin, while the NW sources of Episodes B and C are newly generated and have a different origin. This is discussed further in the next section.

In Figures 6a – c the A1 source presents a small but clear separation from those of A2 and A3. Observed at almost the same time, the A1 centroid at 327 MHz and 09:44 UT is at about 58″ from the A2 centroid at 270 MHz and the A3 centroid at 228 MHz, while the latter two are too close to be separable using NRH data. Thus, the A1 source does not completely overlap with the A2-A3 sources. This indicates that of the three bands of Episode A, A1 may be different from A2 and A3 and the latter two may represent a pair of band split.

In Figure 6 we can compare the locations of different branches. As mentioned above, there is a distance of about 58″ from the A1 centroid to those of A2 and A3, while the latter two basically overlap. The B1 and B2 sources (228 – 150 MHz) are not separable by the NRH. This is mainly due to the small differences in the observational frequencies as well as to the coarse spatial resolution of the NRH. Nevertheless, we can see a clear overall outward propagating trend of the sources of the three episodes (also see Figure 4). The linearly fitted speed is ~ 750 km s^{-1} for the centroids of the Episode A sources and the SE sources of Episode B and C.

5. Combined Analysis of the Radio and EUV Data

In this section, we examine the relationship of the EUV wave with the radio sources on the basis of a combined data analysis.

Using Equation 1 with $X = 0$ and setting the wave speed to be 600 km s^{-1}, we extrapolated the wave profiles at other times as required. Figures 7a – d show the AIA EUV images overlaid by the radio contours and the extrapolated wave profiles for different branches. This allows us to infer the relationship between the radio sources of different type II lanes and the EUV wave. From Figures 7a and b, we see that A1 and A2 are both located at the southern side, very close to the nose of the EUV wave. This indicates that the EUV wave is a shock, according to the general belief that the type II burst is generated by energetic electrons accelerated at a shock (Nelson and Melrose, 1985). In Figures 7c and d the double sources are located on the two sides of the shock nose. The SE sources of Episode B and C and the source of Episode A are in the same section of the shock. This indicates that the SE sources likely are the continuation of the Episode A source. The NW source is coincident with the interaction region of the shock with the mini-streamer-like structure (see the black arrow in Figure 7c). In addition, the onset of the NW source ($\sim$ 09:45:31 UT) is cotemporal with the occurrence of the strong interaction between the shock and the mini-streamer-like structure, as mentioned in Section 2. These observations indicate that the NW source is likely a result of the interaction of the shock with the mini-streamer-like structure.

As described above, both H–F and band-split counterparts are present in this type II burst. To examine the correlation between the shock and the H–F sources of A1 and the band-split sources of B1 and B2, in Figures 8a – d we plot the radio contours and the extrapolated profiles of the shock front at the corresponding times. Similar results of the consistency between the radio sources and the two sides of the shock front are obtained. In Figures 8c – d the band-split sources seem to lie behind the shock front. This may be due to the projection effect. With the present data, it is not possible to infer their actual locations relative to the shock front (*i.e.* upstream or downstream).
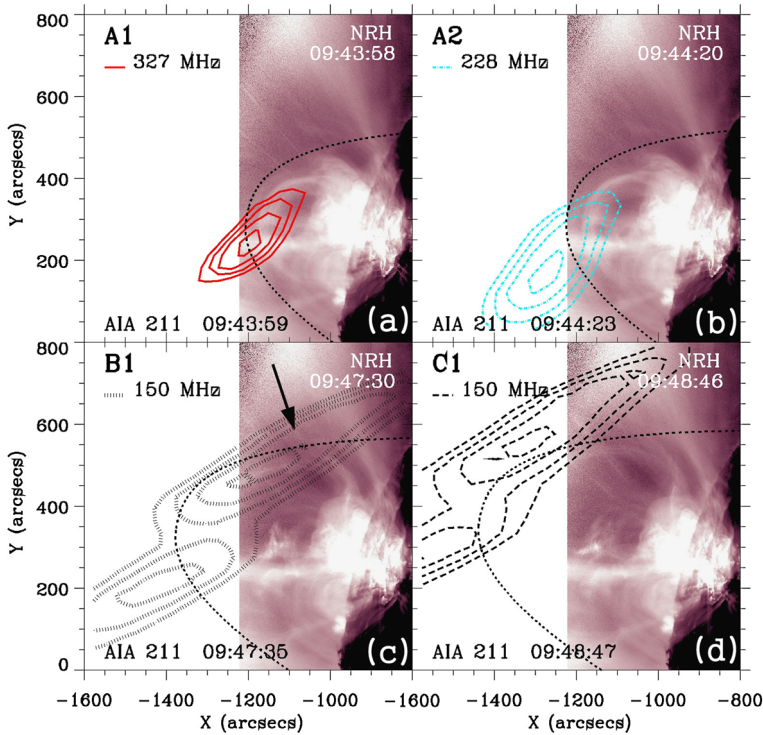
Figure 7 AIA EUV images (211 Å) overlaid by the radio contours of 65, 75, 85, and 95% levels of $T_{\rm Bmax}$ for different branches. The NRH time and frequency combination correspond to the *black plus sign* plotted in Figure 1b. For each panel, the *black dotted curve* indicates the EUV wave front extrapolated from that observed at 09:43:59 UT (see Figure 3c) to the NRH time.

To reveal the relative spatial location of H–F sources and band-split sources, in Figures 8a–d we plot the simultaneously observed H–F (A1–A1F) and band-split (B1–B2) sources. The H sources seem to be ahead of the F sources. The centroid distances are $\sim 200''$ for the pair at $327 - 173$ MHz and $\sim 160''$ for the pair at $298 - 150$ MHz. Although the distances are smaller than the NRH beam widths, the separations are probably real because the two pairs of H–F sources show a consistent centroid-centroid orientation. These observations are consistent with some earlier studies (*e.g.* Robinson and Sheridan, 1982), and are usually interpreted as the stronger scattering and refraction effect on the F emission since its frequency is much more similar (than the H emission) to the oscillation frequency of plasma surrounding the radio source.

Figures 8c and d show that the band-split sources are almost cospatial. The two split bands are at the H branch, and the frequency ratio is ~ 1.2. It is not possible to determine whether the band-split sources are spatially separated because of the relatively low spatial resolution of the radio-imaging heliograph. A more detailed discussion is presented in the following section.

6. Summary and Discussion

A multi-lane type II solar radio burst is a group of type II (narrow band and slow spectral drift) emission lanes observed within a short interval. The starting times and spectral drifts
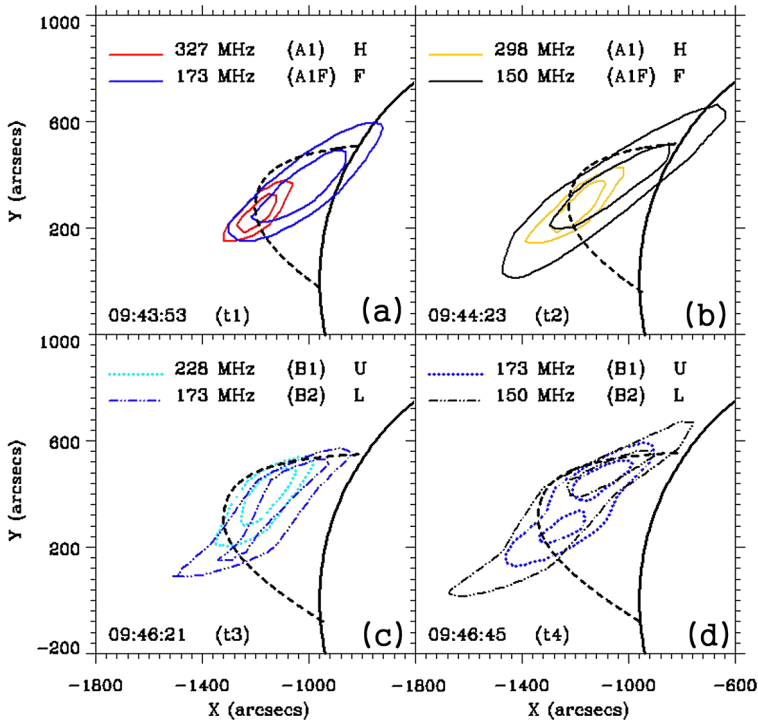
Figure 8 Radio sources (represented by the NRH radio contours of 65 and 85% levels of T_{Bmax}) plotted together for simultaneously observed F–H (**a**–**b**) and band-split (**c**–**d**) pairs. The times selected for the images are presented in Figure 1b (t1 – t4). For each panel, the *black dotted curve* indicates the EUV wave front extrapolated from that observed at 09:43:59 UT (see Figure 3c) to the NRH time.

of different lanes are usually different, and the lanes cannot be fully grouped into H–F and band-split pairs. Earlier studies revealed controversial results regarding the origin of these type II lanes, mainly because of the lack of direct-imaging data of the radio sources. Here we reported a multi-lane type II burst, consisting of more than ten branches, with both H–F and band-split counterparts and three episodes (A, B, and C) according to their spectral drifts and temporal sequence. All lanes are found to be associated with an EUV shock driven by a single CME. The first episode (A) has a single-source morphology, while Episodes B and C have a double-source morphology. It is suggested that the SE source of the double sources of Episodes B and C is the continuation of Episode A (both on the SE side of the shock, close to the shock nose), and the NW source is a newly formed emission source (on the NW side of the shock) that is correlated with and likely caused by the interaction of the CME shock with a nearby mini-streamer-like structure.

These results mean that different sources exist for a single eruption. In earlier studies, both the shock nose and shock flank have been suggested to be the type II sources on the basis of a combined analysis of coronagraph images and radio spectrograph data (*e.g.* Mancuso and Raymond, 2004; Cho *et al.*, 2007, 2008; Feng *et al.*, 2012, 2013; Kong *et al.*, 2012). Using simultaneous radio-imaging data of the NRH and multi-perspective EUV data from STEREO, Chen *et al.* (2014) provided evidence that the CME-coronal ray interaction region is the source of type II bursts. Here, we present another piece of evidence, based on direct-imaging data of the radio source, that the interaction of CMEs with coronal structures

(a mini-streamer-like dense structure in this study) is important for the excitation of type II radio bursts.

According to our analysis, at the early stage of the type II burst, the radio source comes from the SE shock section close to the nose. CMEs normally erupt from closed magnetic arcades. At a heliocentric distance smaller than 2 $R_\odot$, it is possible that the magnetic field remains still closed. This means that the CME front is parallel or quasi-parallel to the top of the arcade. This results in a quasi-perpendicular shock geometry. According to earlier studies, this geometry favors an efficient acceleration of electrons (Wu, 1984; Armstrong, Pesses, and Decker, 1985). In addition, this shock closed-field configuration has recently been demonstrated to be an efficient trap of electrons that greatly enhances the acceleration of electrons via the shock (Kong *et al.*, 2015, 2016). This explains in a qualitative way how a type II source can be generated at or near the nose of a coronal shock.

On the other hand, the CME expands laterally at the flank. This may induce a strong interaction of CMEs with nearby structures, such as coronal rays and/or coronal streamers, which in general are denser than their surroundings and thus have a lower characteristic Alfvén speed. This favors the shock formation or enhancement of a pre-existing shock during its transit through the structures. In addition, the shock may also be quasi-perpendicular along the flank. These factors contribute to an efficient electron acceleration and type II excitation along the shock flank.

Obviously, the observation that different episodes have a different frequency drift is likely due to different source locations along the shock and different structures involved. This study thus demonstrates that multiple type II episodes with different drifts can be generated even though the burst is associated with a single CME. Many earlier studies on type II bursts were based on some experimental coronal density models. These density models cannot explain all episodes of the burst under study. In particular, they are not applicable when the spectral drift is mainly accounted for by the non-radial transit of the shock and the corresponding density gradient across nearby coronal structures.

In this study, we also examined the spatial relation of simultaneously observed sources of H–F counterparts and band-split pairs. The H–F sources do not completely overlap. The difference of the H–F sources is traditionally interpreted as a result of strong scattering and refraction effect on the fundamental emission. For the band-split sources, only rare studies exist to spatially resolve the sources of the split bands (*e.g.* Zimovets *et al.*, 2012; Zucca *et al.*, 2014b) with details of the eruptive structure. Here, with one such observation, we showed that the band-split sources basically overlap, and both are in line with the front of the EUV shock.

The band split of type II radio bursts is a very intriguing phenomenon that is not fully understood yet. The well-known upstream-downstream scenario proposed by Smerd, Sheridan, and Stewart (1974) is an attractive assumption, but no strong observational and theoretical support is available (see Du *et al.*, 2014, for a brief review of current scenarios, and Eselevich, Eselevich, and Zimovets, 2013, 2016, for another scenario involving both the flare blast wave and the CME-driven piston shock wave). Nevertheless, many observational studies are based on this assumption to further deduce the shock compression ratio and coronal magnetic field strength, such as the studies by Vršnak *et al.* (2002), Cho *et al.* (2007), and many others. Clues that apparently contradict this interpretation have been presented by Du *et al.* (2014, 2015). Note that Du *et al.* (2014) reported a medium level of polarization of the split bands, observed at the decametric wavelength using *Nançay Decameter Array* (NDA) data. We acknowledge that the polarization data used there are not well calibrated to our knowledge, and the polarization levels reported may be inaccurate.

The NRH spatial resolution is mainly determined by the beam width. Around 150–300 MHz, the NRH beams are as wide as a few to several arcminutes. Observationally,

the split bands present a very similar behavior in the temporal profiles of their dynamic spectra. This means that their sources probably do not lie far away from each other. The upstream-downstream scenario predicts that the low-frequency component (LFC) and high-frequency component (HFC) sources of a band split are located upstream and downstream of the shock, respectively. Thus, the LFC is spatially separated from (slightly higher than) the HFC source, butt their distance is likely too small to be spatially resolved by the NRH, given its relatively large beam width. Projection effects, which always exist for 2D imaging of the Sun, can deteriorate the situation.

Note that both Zimovets *et al.* (2012) and Zucca *et al.* (2014b) have used NRH data to spatially resolve the sources of split bands. They presented evidence that the centroid of the LFC source may be slightly higher than that of the HFC source. This supports the upstream-downstream scenario. In our study, the separation of LFC and HFC centroids is much smaller than the NRH beam widths. In addition, the shape of the sources is more complex, so that it may be inappropriate to represent the source solely with its centroid. Thus, we conclude that the sources of the band split in our event are not separable with the NRH.

Many earlier studies of type II sources have had to rely on experimental density models of the corona, so as to convert the emission frequencies into heights of coronal shock and thus infer the shock propagation speed. This treatment was unable to yield appropriate results when the corona was highly structured and dynamically evolved with time. Zucca *et al.* (2014a) developed a method to partially resolve this issue by deducing two-dimensional maps of the coronal density, the magnetic field strength, and thus the Alfvén speed, on the basis of the EUV and magnetic data from SDO, and the polarization brightness measurement from SOHO/LASCO. They concluded that the two flanks of the CME front are possible sources of the type II radio burst. Nevertheless, if further considering the three-dimensional effect, the radio sources could come from the whole circle of intersection of the CME front with their frequency contour (see their Figure 12). Thus, the study shows that without direct imaging of the radio sources, it is difficult if not impossible to determine the location of type II sources. In our study here, we took advantage of the simultaneous NRH radio and AIA EUV imaging data and directly determined the relative location of the EUV shock wave and various source components as well as some general morphological evolution. This again highlights the necessity of direct-imaging data at radio wavelength to unravel the secret of the type II origin.

Disclosure of Potential Conflicts of Interest   The authors declare that they have no conflicts of interest.

References

Armstrong, T.P., Pesses, M.E., Decker, R.B.: 1985, Shock drift acceleration. In: *AGU Monograph Ser.* **35**, American Geophysical Union, Washington, 271. DOI. ADS.

Baars, J.W.M., Genzel, R., Pauliny-Toth, I.I.K., Witzel, A.: 1977, The absolute spectrum of CAS A – an accurate flux density scale and a set of secondary calibrators. *Astron. Astrophys.* **61**, 99. ADS.

Brueckner, G.E., Howard, R.A., Koomen, M.J., Korendyke, C.M., Michels, D.J., Moses, J.D., Socker, D.G., Dere, K.P., Lamy, P.L., Llebaria, A., Bout, M.V., Schwenn, R., Simnett, G.M., Bedford, D.K., Eyles, C.J.: 1995, The Large Angle Spectroscopic Coronagraph (LASCO). *Solar Phys.* **162**, 357. DOI. ADS.

Chen, Y., Du, G., Feng, L., Feng, S., Kong, X., Guo, F., Wang, B., Li, G.: 2014, A solar type II radio burst from coronal mass ejection-coronal ray interaction: simultaneous radio and extreme ultraviolet imaging. *Astrophys. J.* **787**, 59. DOI. ADS.

Cho, K.-S., Lee, J., Moon, Y.-J., Dryer, M., Bong, S.-C., Kim, Y.-H., Park, Y.D.: 2007, A study of CME and type II shock kinematics based on coronal density measurement. *Astron. Astrophys.* **461**, 1121. DOI. ADS.

Cho, K.-S., Bong, S.-C., Kim, Y.-H., Moon, Y.-J., Dryer, M., Shanmugaraju, A., Lee, J., Park, Y.D.: 2008, Low coronal observations of metric type II associated CMEs by MLSO coronameters. *Astron. Astrophys.* **491**, 873. DOI. ADS.

Cho, K.-S., Bong, S.-C., Moon, Y.-J., Shanmugaraju, A., Kwon, R.-Y., Park, Y.D.: 2011, Relationship between multiple type II solar radio bursts and CME observed by STEREO/SECCHI. *Astron. Astrophys.* **530**, A16. DOI. ADS.

Domingo, V., Fleck, B., Poland, A.I.: 1995, The SOHO mission: an overview. *Solar Phys.* **162**, 1. DOI. ADS.

Du, G., Chen, Y., Lv, M., Kong, X., Feng, S., Guo, F., Li, G.: 2014, Temporal spectral shift and polarization of a band-splitting solar type II radio burst. *Astrophys. J. Lett.* **793**, L39. DOI. ADS.

Du, G., Kong, X., Chen, Y., Feng, S., Wang, B., Li, G.: 2015, An observational revisit of band-split solar type-II radio bursts. *Astrophys. J.* **812**, 52. DOI. ADS.

Eselevich, V.G., Eselevich, M.V., Zimovets, I.V.: 2013, Blast-wave and piston shocks connected with the formation and propagation of a coronal mass ejection. *Astron. Rep.* **57**, 142. DOI. ADS.

Eselevich, V.G., Eselevich, M.V., Zimovets, I.V.: 2016, Possible reasons for the frequency splitting of the harmonics of type II solar radio bursts. *Astron. Rep.* **60**, 163. DOI. ADS.

Feng, S.W., Chen, Y., Kong, X.L., Li, G., Song, H.Q., Feng, X.S., Liu, Y.: 2012, Radio signatures of coronal-mass-ejection-streamer interaction and source diagnostics of type II radio burst. *Astrophys. J.* **753**, 21. DOI. ADS.

Feng, S.W., Chen, Y., Kong, X.L., Li, G., Song, H.Q., Feng, X.S., Guo, F.: 2013, Diagnostics on the source properties of a type II radio burst with spectral bumps. *Astrophys. J.* **767**, 29. DOI. ADS.

Feng, S.W., Du, G.H., Chen, Y., Kong, X.L., Li, G., Guo, F.: 2015, Simultaneous radio and EUV imaging of a multi-lane coronal type II radio burst. *Solar Phys.* **290**, 1195. DOI. ADS.

Gergely, T.E., Kundu, M.R., Wu, S.T., Dryer, M., Smith, Z., Stewart, R.T.: 1984, A multiple type-II burst associated with a coronal transient and its MHD simulation. *Adv. Space Res.* **4**, 283. DOI. ADS.

Ginzburg, V.L., Zhelezniakov, V.V.: 1958, On the possible mechanisms of sporadic solar radio emission (radiation in an isotropic plasma). *Soviet Astron.* **2**, 653. ADS.

Gopalswamy, N., Thompson, W.T., Davila, J.M., Kaiser, M.L., Yashiro, S., Mäkelä, P., Michalek, G., Bougeret, J.-L., Howard, R.A.: 2009, Relation between type II bursts and CMEs inferred from STEREO observations. *Solar Phys.* **259**, 227. DOI. ADS.

Howard, R.A., Moses, J.D., Vourlidas, A., Newmark, J.S., Socker, D.G., Plunkett, S.P., Korendyke, C.M., Cook, J.W., Hurley, A., Davila, J.M., Thompson, W.T., St Cyr, O.C., Mentzell, E., Mehalick, K., Lemen, J.R., Wuelser, J.P., Duncan, D.W., Tarbell, T.D., Wolfson, C.J., Moore, A., Harrison, R.A., Waltham, N.R., Lang, J., Davis, C.J., Eyles, C.J., Mapson-Menard, H., Simnett, G.M., Halain, J.P., Defise, J.M., Mazy, E., Rochus, P., Mercier, R., Ravet, M.F., Delmotte, F., Auchere, F., Delaboudiniere, J.P., Bothmer, V., Deutsch, W., Wang, D., Rich, N., Cooper, S., Stephens, V., Maahs, G., Baugh, R., McMullin, D., Carter, T.: 2008, Sun Earth connection coronal and heliospheric investigation (SECCHI). *Space Sci. Rev.* **136**, 67. DOI. ADS.

Kerdraon, A., Delouis, J.-M.: 1997, The Nançay Radioheliograph. In: Trottet, G. (ed.) *Coronal Physics from Radio and Space Observations*, *Lec. Notes Phys.*, **483**, Springer, Berlin, 192. DOI. ADS.

Kong, X.L., Chen, Y., Li, G., Feng, S.W., Song, H.Q., Guo, F., Jiao, F.R.: 2012, A broken solar type II radio burst induced by a coronal shock propagating across the streamer boundary. *Astrophys. J.* **750**, 158. DOI. ADS.

Kong, X., Chen, Y., Guo, F., Feng, S., Wang, B., Du, G., Li, G.: 2015, The possible role of coronal streamers as magnetically closed structures in shock-induced energetic electrons and metric type II radio bursts. *Astrophys. J.* **798**, 81. DOI. ADS.

Kong, X., Chen, Y., Guo, F., Feng, S., Du, G., Li, G.: 2016, Electron acceleration at a coronal shock propagating through a large-scale streamer-like magnetic field. *Astrophys. J.* **821**, 32. DOI. ADS.

Lemen, J.R., Title, A.M., Akin, D.J., Boerner, P.F., Chou, C., Drake, J.F., Duncan, D.W., Edwards, C.G., Friedlaender, F.M., Heyman, G.F., Hurlburt, N.E., Katz, N.L., Kushner, G.D., Levay, M., Lindgren, R.W., Mathur, D.P., McFeaters, E.L., Mitchell, S., Rehse, R.A., Schrijver, C.J., Springer, L.A., Stern, R.A., Tarbell, T.D., Wuelser, J.-P., Wolfson, C.J., Yanari, C., Bookbinder, J.A., Cheimets, P.N., Caldwell, D., Deluca, E.E., Gates, R., Golub, L., Park, S., Podgorski, W.A., Bush, R.I., Scherrer, P.H., Gummin, M.A., Smith, P., Auker, G., Jerram, P., Pool, P., Soufli, R., Windt, D.L., Beardsley, S., Clapp, M., Lang, J., Waltham, N.: 2012, The Atmospheric Imaging Assembly (AIA) on the Solar Dynamics Observatory (SDO). *Solar Phys.* **275**, 17. DOI. ADS.

Liu, Y., Luhmann, J.G., Bale, S.D., Lin, R.P.: 2009, Relationship between a coronal mass ejection-driven shock and a coronal metric type II burst. *Astrophys. J. Lett.* **691**, L151. DOI. ADS.

Mancuso, S., Raymond, J.C.: 2004, Coronal transients and metric type II radio bursts. I. Effects of geometry. *Astron. Astrophys.* **413**, 363. DOI. ADS.

Melrose, D.B.: 1980, The emission mechanisms for solar radio bursts. *Space Sci. Rev.* **26**, 3. DOI. ADS.

Nelson, G.J., Melrose, D.B.: 1985, In: McLean, D.J., Labrum, N.R. (eds.) *Type II Bursts*, 333. ADS.

Neupert, W.M.: 1968, Comparison of solar X-ray line emission with microwave emission during flares. *Astrophys. J. Lett.* **153**, L59. DOI. ADS.

Payne-Scott, R., Yabsley, D.E., Bolton, J.G.: 1947, Relative times of arrival of bursts of solar noise on different radio frequencies. *Nature* **160**, 256. DOI. ADS.

Pesnell, W.D., Thompson, B.J., Chamberlin, P.C.: 2012, The Solar Dynamics Observatory (SDO). *Solar Phys.* **275**, 3. DOI. ADS.

Robinson, R.D., Sheridan, K.V.: 1982, A study of multiple type II solar radio events. *Proc. Astron. Soc. Aust.* **4**, 392. ADS.

Shanmugaraju, A., Moon, Y.-J., Cho, K.-S., Kim, Y.-H., Dryer, M., Umapathy, S.: 2005, Multiple type II solar radio bursts. *Solar Phys.* **232**, 87. DOI. ADS.

Smerd, S.F., Sheridan, K.V., Stewart, R.T.: 1974, On split-band structure in type II radio bursts from the Sun (presented by S.F. Smerd). In: Newkirk, G.A. (ed.) *Coronal Disturbances*, *IAU Symp.* **57**, 389. ADS.

Song, H.Q., Chen, Y., Zhang, J., Cheng, X., Fu, H., Li, G.: 2015, Acceleration phases of a solar filament during its eruption. *Astrophys. J. Lett.* **804**, L38. DOI. ADS.

Vasanth, V., Umapathy, S., Vršnak, B., Žic, T., Prakash, O.: 2014, Investigation of the coronal magnetic field using a type II solar radio burst. *Solar Phys.* **289**, 251. DOI. ADS.

Vršnak, B., Aurass, H., Magdalenić, J., Gopalswamy, N.: 2001, Band-splitting of coronal and interplanetary type II bursts. I. Basic properties. *Astron. Astrophys.* **377**, 321. DOI. ADS.

Vršnak, B., Magdalenić, J., Aurass, H., Mann, G.: 2002, Band-splitting of coronal and interplanetary type II bursts. II. Coronal magnetic field and Alfvén velocity. *Astron. Astrophys.* **396**, 673. DOI. ADS.

Wu, C.S.: 1984, A fast Fermi process – energetic electrons accelerated by a nearly perpendicular bow shock. *J. Geophys. Res.* **89**, 8857. DOI. ADS.

Zhang, J., Dere, K.P., Howard, R.A., Kundu, M.R., White, S.M.: 2001, On the temporal relationship between coronal mass ejections and flares. *Astrophys. J.* **559**, 452. DOI. ADS.

Zimovets, I.V., Sadykov, V.M.: 2015, Spatially resolved observations of a coronal type II radio burst with multiple lanes. *Adv. Space Res.* **56**, 2811. DOI. ADS.

Zimovets, I., Vilmer, N., Chian, A.C.-L., Sharykin, I., Struminsky, A.: 2012, Spatially resolved observations of a split-band coronal type II radio burst. *Astron. Astrophys.* **547**, A6. DOI. ADS.

Zucca, P., Carley, E.P., Bloomfield, D.S., Gallagher, P.T.: 2014a, The formation heights of coronal shocks from 2D density and Alfvén speed maps. *Astron. Astrophys.* **564**, A47. DOI. ADS.

Zucca, P., Pick, M., Démoulin, P., Kerdraon, A., Lecacheux, A., Gallagher, P.T.: 2014b, Understanding coronal mass ejections and associated shocks in the solar corona by merging multiwavelength observations. *Astrophys. J.* **795**, 68. DOI. ADS.